Probabilistic model of bone structure based on CT scan data and validation of simulation results using the Finite Cell Method

J. Luque, I. Papaioannou & D. Straub
Engineering Risk Analysis Group, Technische Universität München, Germany

M. Ruess
Aerospace Structures & Computational Mechanics, Delft University of Technology, The Netherlands

D. Schillinger
Institute for Computational Engineering and Sciences, The University of Texas, USA

ABSTRACT: A probabilistic model of bone structure in the trabecular region of the femur head is constructed. In a first step, a probabilistic model for the bone density based on computed tomography (CT) scan data is developed. The data consist of a number of cubes cut from fresh-frozen bones belonging to three different patients. The model accounts for the spatial variability of the bone structure as well as the correlation between samples (inter-sample correlation). Based on the statistical analysis of the data, a homogeneous Gaussian field with separable autocorrelation coefficient function is developed for modeling the bone structure. The Finite Cell Method (FCM) is used for estimation of the mechanical properties of the bone. This method has shown advantages in terms of efficiency and accuracy compared to the classical finite element method for this type of applications. Monte Carlo samples of the mechanical properties of the bone are simulated based on the probabilistic model of the bone density. For each realization of the random field, density values at each location are obtained and further mapped to material values through empirical relationships. Furthermore, the homogenized material properties are computed using the FCM assuming an isotropic material. The sample elasticity moduli are compared with the ones obtained experimentally from laboratory tests in order to validate the applicability of the material models at different scales.

1 INTRODUCTION

The mechanical behavior of human bones has been studied using both experimental and computational techniques. One common computational approach is the Finite Element Method (FEM). However, as discussed in (Ruess et al. 2012), the application of classical h-version FEM to bone simulation may lead to results with low accuracy and efficiency. The Finite Cell Method (FCM) offers an alternative, which provides more accurate solutions with similar or even lower computational cost (Ruess et al. 2012, Schillinger et al. 2012). Bone experiments are subject to multiple source of uncertainty and randomness. These include spatial heterogeneity of bone properties, measurement device noise, scale of the sample, and uncertainties in material models. In numerical simulation of bones these uncertainties are typically neglected. This assumption can lead to significant differences between simulation and experimental results. The aim of this paper is to propose an alternative probabilistic model approach, which addresses the spatial heterogeneity of the bone structure through random fields.

In this paper, the density of the trabecular region of human fresh-frozen femurs is analyzed and modeled as a homogeneous Gaussian random field, based on quantitative computer tomography (CT) scan data. An algorithm for the generation of random bone samples is developed and it is used in a Monte Carlo setting for the estimation of the mechanical properties of the bone. Correlations of attenuation values (i.e. the outcome of the CT scanner and related to the bone density) within and between samples (i.e. intra- and inter-sample correlations) are distinguished. For each sample, the density values at each location are mapped to material values through empirical relationships and the homogenized mechanical properties are estimated applying the FCM. Different material relationships are used and compared with the experimental results from laboratory tests in order to assess their accuracy at different scales.

2 EXPERIMENTAL DATA

Three different fresh-frozen femur bones were analyzed using a CT scanner (Grande 2013). Several cubic samples (see Table 1) from the trabecular region were cut from each bone and scanned. Each sample had an approximate size of 7 mm × 6 mm × 6 mm and the information was provided in a 3-dimensional matrix that contained the attenuation values for each location according to the predefined resolution for the sample (Fig. 1).

Table 1. Bone samples from laboratory

Patient	Samples	Matrix size	Resolution of voxel [mm]
P1	8		
P2	10	50×40×17	0.1465×0.1465×0.335
P3	4		

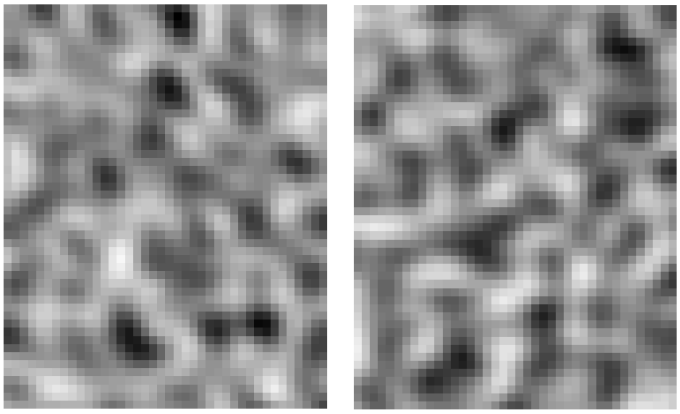

Figure 1. Example of attenuations from two different "slices" of scanned bones.

The measurements included in the matrix correspond to different locations in the bone sample based on a Cartesian grid. Some of the original bone samples were larger than the size defined in Table 1, however their domain was truncated for standardization purposes.

The setting of the CT scan is illustrated in Figure 2. The CT scanner generates a set of attenuation measurements that correspond to the density of the scanned object at different locations. These measurements are presented in Hounsfield Units (HU), where a value of −1000 corresponds to air and 0 to water. The calibration phantom provides five reference materials (the circular regions depicted in Fig. 2) with known densities for estimation of the density of the bone at the moment of the scan (QCT PRO™ 2008). Based on the known K_2HPO_4 density values (or Bone Mineral Density, BMD) of the phantom materials, the scanned sample density is transformed from HU to BMD through linear regression. Based on the procedure stated in (QCT PRO™ 2008), an excellent linear relation ($R^2 = 0.998$) between attenuation value μ_{CT} (in HU) and the density ρ_{BMD} (in g⁄cm^3) of the bone samples analyzed was obtained:

$$\rho_{\mathrm{BMD}} = (\mu_{CT} + 8.26)/1134 \quad (1)$$

Estimation of the elasticity modulus (E) of each sample was carried out in the laboratory using two different methods: Extensometer Film Method (EFM) and the Pressure Film Method (PFM). The experimental results were performed by the Department of Orthopedics and Sports Medicine at TU Munich (Grande 2013). Comparison between the average ρ_{BMD} of each sample and corresponding experimental E is plotted in Figure 3. This information will be used to validate the results obtained from the simulations.

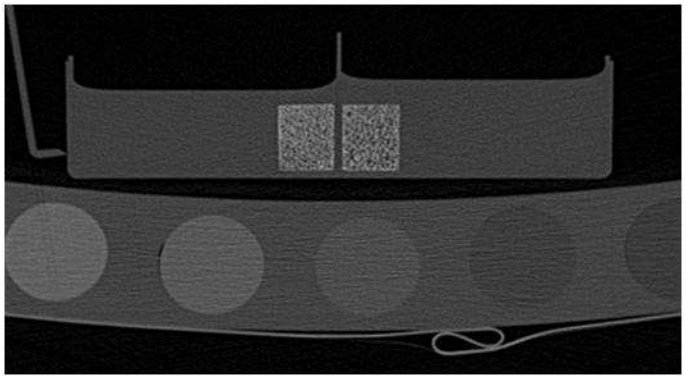

Figure 2. Example of a CT scan image. Circular regions correspond to the reference samples with known density whereas the squared regions correspond to bone samples.

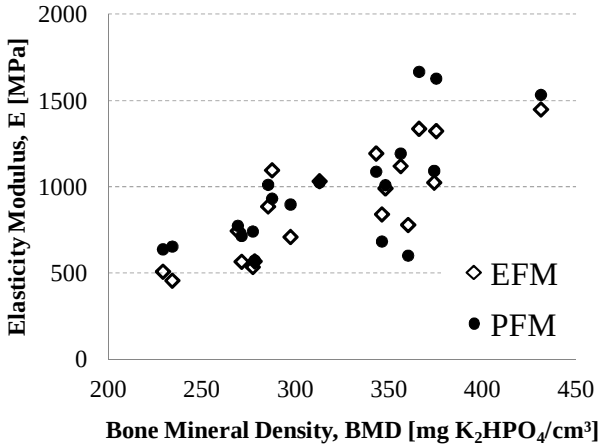

Figure 3. Experimental relation between the density and the elasticity modulus.

3 STOCHASTIC MODEL

3.1 *Definition of the random field*

Most physical systems present spatial variability accompanied by interrelationships among the elements in different locations. Some of these systems have properties or variables that might be difficult to model using deterministic relations due to their complexity or the number of parameters affecting them. Random fields represent an alternative for modeling those systems with the aim of representing their variability using a minimum number of parameters (Vanmarcke 2010).

A random field $X(\mathbf{z})$, where $\mathbf{z} \in \Omega$, $\Omega \subset \mathbb{R}^3$, is defined as a collection of random variables indexed by a continuous location parameter $\mathbf{z}$. $X(\mathbf{z})$ is called Gaussian if the random vector $\{X(\mathbf{z}_1), \dots, X(\mathbf{z}_n)\}$ is jointly Gaussian for any n number of points and locations $\{\mathbf{z}_1, \dots, \mathbf{z}_n\}$. When the joint distribution of $\{X(\mathbf{z}_1), \dots, X(\mathbf{z}_n)\}$ is the same as the one of $\{X(\mathbf{z}_1 + \boldsymbol{\delta}), \dots, X(\mathbf{z}_n + \boldsymbol{\delta})\}$ for any translation vector $\boldsymbol{\delta}$, then $X(\boldsymbol{z})$ is said to be homogenous. This property means that the correlation between two points is defined

through their relative rather than their absolute position.

Considering the repetitive and relative homogenous behavior of the bone structure (Fig. 1), it is possible to model the attenuation value $X(\mathbf{z})$ over the bone domain as a random field. Statistical analysis of the scanned samples (e.g. mean, standard deviation, empirical Cumulative Density Function, CDF) was carried out in order to justify the assumption of a homogenous Gaussian field for describing the attenuation value (Fig. 4).

The autocorrelation coefficient function $\rho_X(\mathbf{z}_1, \mathbf{z}_2)$ describes the correlation between two locations of the random field. For homogeneous random fields, ρ_X is a function of the translation vector $\boldsymbol{\delta}$ between two locations. $X(\mathbf{z})$ is anisotropic because it is expected that the autocorrelation in the longitudinal direction of the bone will be larger than the autocorrelation in the other two directions due to its structural design. We assume a separable autocorrelation function based on the empirical autocorrelations estimated separately for each direction.

The autocorrelation coefficient function between attenuation values at locations $\mathbf{z}_1$ and $\mathbf{z}_2$, is expressed as:

$$\rho_X(\mathbf{z}_1, \mathbf{z}_2) = \rho_{X,i}(\delta_i) \cdot \rho_{X,j}(\delta_j) \cdot \rho_{X,k}(\delta_k) \quad (2)$$

where $\boldsymbol{\delta} = \mathbf{z}_2 - \mathbf{z}_1 = [\delta_i, \delta_j, \delta_k]$ is the translation vector between the two locations and functions $\rho_{X,i}$, $\rho_{X,j}$ and $\rho_{X,k}$ are the autocorrelation coefficient functions in each main direction.

3.2 *Inter- and intra-sample correlations*

In general, it is expected that autocorrelation coefficient functions of individual bone samples should tend to zero as the distance between two locations increases. We define this within-correlation as intra-sample correlation, since its value is obtained using only measurements from a single sample. However, the correlation estimated by several samples does not necessarily tend to zero. This is mainly caused by an additional "noise" produced by the scanner itself and some environmental conditions at the moment of the experiment (e.g. temperature, humidity). This effect is independent of the bone material properties and will be defined as the inter-sample correlation.

In order to separate between inter- and intra-sample correlations, the following relation is defined:

$$X(\mathbf{z}) = X'(\mathbf{z}) + Y \quad (3)$$

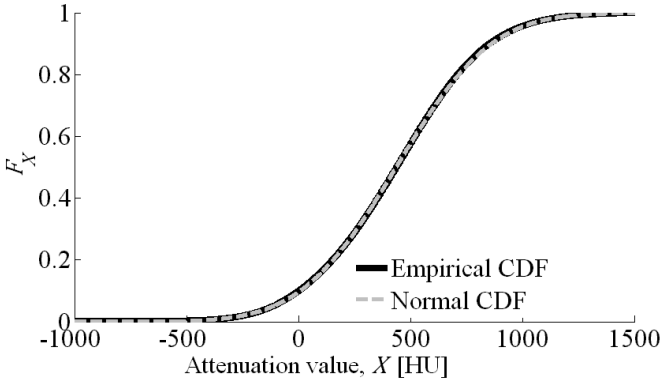

Figure 4. Comparison between the empirical CDF of the attenuation values and the corresponding Normal distribution with the same mean and standard deviation.

where $X(\mathbf{z})$ is the random field associated to the attenuation values (in HU) obtained from the CT scanner, $X'(\mathbf{z})$ is the attenuation value containing only the intra-sample correlation and Y is a zero mean random variable independent of $X'(\mathbf{z})$ that models the inter-sample correlation. Hence, the autocorrelation and autocovariance functions of $X'(\mathbf{z})$ will tend to zero as the distance between two locations increases.

The correlation between attenuation values $X(\mathbf{z})$ at two locations $\mathbf{z}$ and $\mathbf{z} + \boldsymbol{\delta}$ reads

$$\rho\big(X(\mathbf{z}), X(\mathbf{z}+\boldsymbol{\delta})\big) = \rho_X(\boldsymbol{\delta})$$

$$= \left(\mathrm{cov}[X'(\mathbf{z}), X'(\mathbf{z}+\boldsymbol{\delta})] + \sigma_Y^2\right) / \left(\sigma_{X'}^2 + \sigma_Y^2\right) \quad (4)$$

It can be seen that if the norm of the translation vector $\boldsymbol{\delta}$ increases, then $\rho_X(\boldsymbol{\delta})$ tends to

$$\varepsilon = \sigma_Y^2 / \left(\sigma_{X'}^2 + \sigma_Y^2\right) \quad (5)$$

The value ε will be called the inter-sample correlation. Combining equations (3) and (5), $\sigma_{X'}$ and σ_Y can be expressed as a function of σ_X and ε:

$$\sigma_Y = \sqrt{\varepsilon} \cdot \sigma_X \quad (6)$$

$$\sigma_{X'} = \sqrt{1-\varepsilon} \cdot \sigma_X \quad (7)$$

From equations (6) and (7), it follows that the auto-correlation coefficient function of $X'(\mathbf{z})$ is:

$$\rho_{X'}(\boldsymbol{\delta}) = \frac{\rho_X(\boldsymbol{\delta}) - \varepsilon}{1-\varepsilon} \quad (8)$$

Thus, the autocorrelation coefficient function $\rho_{X'}$ can be obtained in terms of the function ρ_X and the inter-sample correlation.

3.3 *Empirical autocorrelation coefficient functions*

Based on the scanned bone samples, the empirical autocorrelation coefficient functions for each sample on each main direction (defined by the shape of the sample) are plotted in Figure 5. Direction *k* corresponds to the longitudinal direction of the bone.

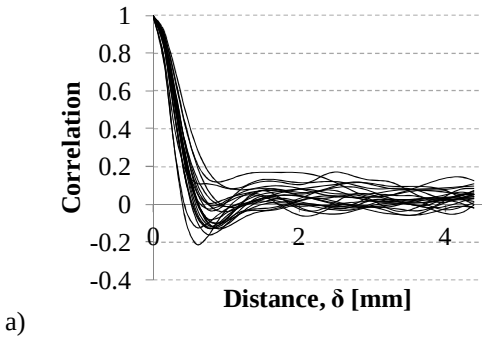

a)

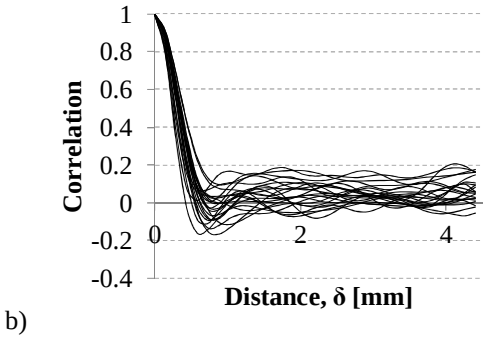

b)

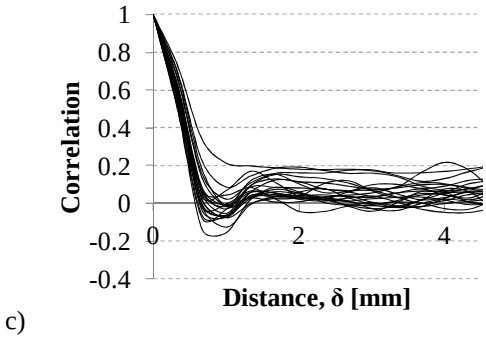

c)

Figure 5. Empirical autocorrelation functions for each sample and each main direction. Plots a), b) and c) correspond to directions *i*, *j* and *k*, respectively.

These functions have an oscillatory behavior and, in average, tend to zero as the distance between points increases. However, if all samples are included in the estimation then the empirical autocorrelation coefficient function presents a different trend (Fig. 6) due to the reasons already explained in Section 3.2.

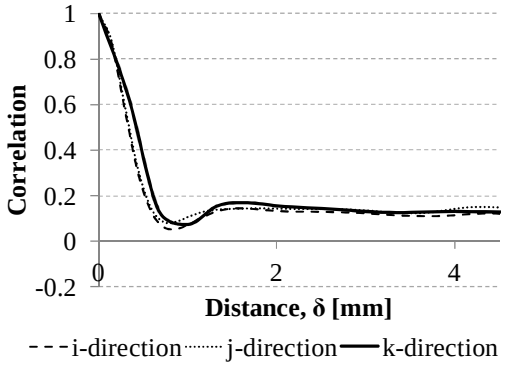

Figure 6. Autocorrelation coefficient function for each main direction using all available information.

Using equations (6) and (8), it is possible to obtain the standard deviation of Y and the function $\rho_{X'}$ (i.e. without inter-sample correlation), respectively (Fig. 7 and Table 2). These are used for generating random realizations of the attenuation values through sampling $X'(\mathbf{z})$ and Y and applying equation (3). The scales of fluctuation in each direction i, j and k are estimated as 0.54mm, 0.65mm and 0.34mm, respectively. These are scalar measures of the spatial dependence corresponding to the integrals of the autocorrelation coefficient function in each direction (Vanmarcke 2010).

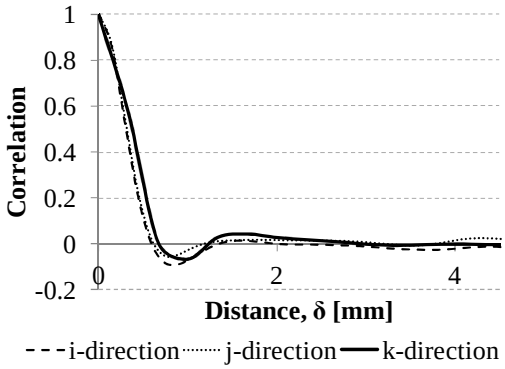

Figure 7. Autocorrelation coefficient function without inter-sample correlation.

Table 2. Estimated parameters of X, X' and Y

Variable	Parameter	Value
X	ε	0.13
	μ_X	435.84 HU
	σ_X	333.7 HU
	ρ_X	See Figure 6
X'	$\mu_{X'}$	435.84 HU
	$\sigma_{X'}$	311.25 HU
	$\rho_{X'}$	See Figure 7
Y	σ_Y	120.32 HU

3.4 *Simulation of random bone samples*

In order to simulate bone samples using the information from laboratory, realizations of $X'(\mathbf{z})$ and Y are generated. However, it is very unlikely that the covariance matrix $\Sigma_{X'X'}$ is positive definite due to the fact that empirical autocorrelations are being used. Moreover, as the size of the random field defined by $X'(\mathbf{z})$ increases, the required computation time and memory allocation present additional difficulties.

In this paper, a truncation of the spectral decomposition of $X'(\mathbf{z})$ together with a sequential Gaussian simulation are used to generate the random bone samples. The algorithm for obtaining a realization of X is depicted in Figure 8 and explained below.

Given a partition $\{\Omega_i\}_{i=1,\dots,M}$ of the domain of interest Ω, the covariance matrix $\Sigma^{(1)}$ (i.e. related to the domain Ω_1) is constructed using the empirical correlations obtained from the data. Then its N largest positive eigenvalues (and their corresponding ei-

genvectors) are used in the spectral decomposition of $X'^{(1)}$ for the generation of samples in Ω_1.

For each of the remaining domains Ω_i, $i > 1$, samples are generated conditional on $\Omega_1, \dots, \Omega_k$, with $k = 1, \dots, i-1$. The matrix $\Sigma^{(i)}$ is the conditional covariance matrix in domain Ω_i given all the previous simulated domains and can be derived analytically, due to the assumption of normality. Computer memory consumption starts to be an issue as the algorithm advances due to the fact that correlations between elements from the domain Ω_i and all previous simulated domains need to be considered. To avoid this problem, one can exploit the fact that most of these correlations are close to zero as the distance between locations increases. We define ξ as a negligible correlation limit (i.e. small enough correlation to be assumed equal to zero) and $\Omega^*_{[i-1]}$ as the set of domains whose correlations with respect to locations in Ω_i are not negligible (i.e. all elements of $\Omega^*_{[i-1]}$ have correlation larger than ξ with at least one element of Ω_i). Then the matrix $\Sigma^{(i)}$ can be approximated by conditioning only to the domain $\Omega^*_{[i-1]}$ instead of all previous simulated domains, leading to considerably smaller matrices. The spectral representation is now performed using this approximation of the conditional covariance matrix.

After the simulation of the attenuation values for the whole domain Ω, the last step is the simulation of variable Y in order to include the inter-sample correlation. This variable is a scalar that has to be added to all locations of the simulated X'. As an example, some realizations of the attenuation values are shown in Figure 9.

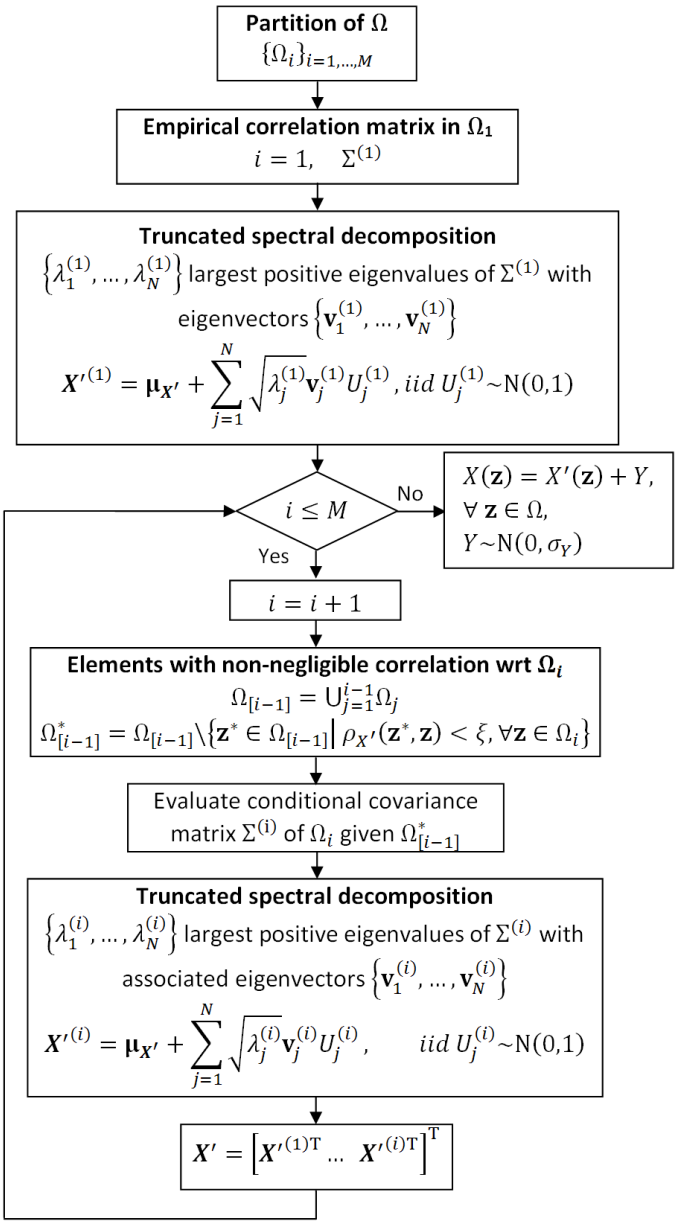

Figure 8. Algorithm for generating random bone samples.

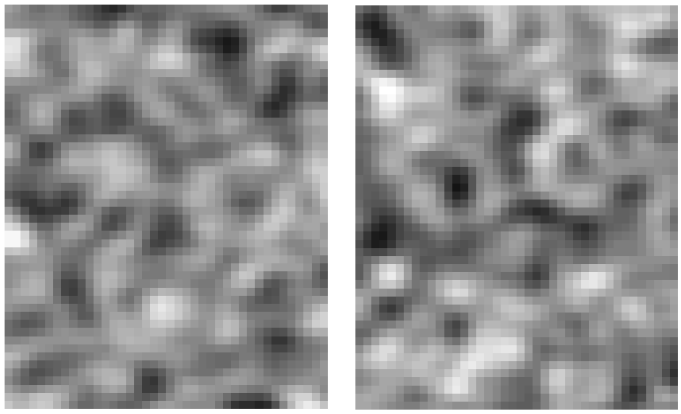
Figure 9. Example of attenuations from two different "slices" of simulated bones.

4 FINITE CELL METHOD

The Finite Cell Method is a fictitious domain method of higher approximation order. The principal idea of the method is independent of the applied Ansatz space and so far has been successfully tested for integrated Legendre polynomials (Schillinger et al. 2012) as known from the p-version of the finite element method as well as for B-splines (Schillinger et al. 2012) and NURBS (Ruess et al. 2013).

The method shows its strength in particular for heterogeneous materials and multiple material interfaces which makes it well suited for the analysis of bone tissue. Based on the principle of virtual displacements, the FCM satisfies the governing integral equations within a simplified domain of computation. The method embeds the potentially complex domain of interest Ω in an extended simulation domain $\Omega_{ext} \subseteq \Omega_{fict}$ that is generated on a Cartesian grid (Fig. 10).

Each grid cell represents a high-order hexahedral element. Cells that are completely outside Ω do not contribute to the elasticity behavior of the structure and are therefore omitted.

The boundary of the fictitious domain Ω_{fict} is assumed to be traction-free. Prescribed forces $\mathbf{t}_0$ and prescribed displacements $\mathbf{u}_0$ are directly applied to the boundary Γ_t and Γ_u, respectively, of the true domain Ω where

$$\Gamma_t \cup \Gamma_u = \Gamma \quad \text{and} \quad \Gamma_t \cap \Gamma_u = \emptyset \tag{9}$$

with Γ denoting the complete boundary of Ω.

The embedding character of the fictitious domain method requires a penalization of the stresses and volume forces in the fictitious extension domain Ω_{fict} to confine their influence on the true solution domain Ω. Following Hooke's law for linear elastic material, the stress-strain relation is coupled by the elasticity tensor $\mathbf{C}$.

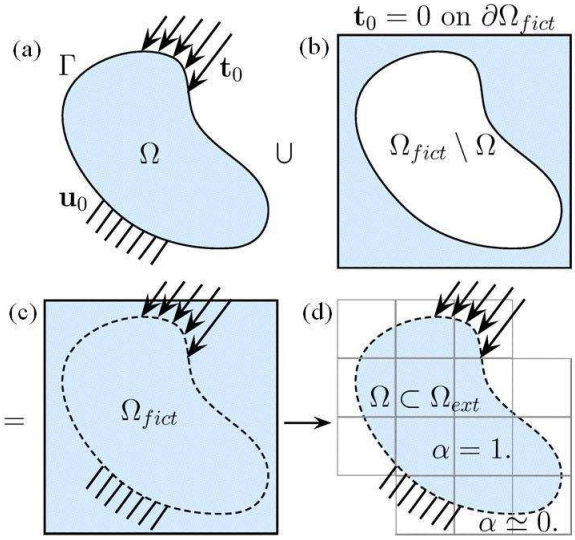

Figure 10. (a) Physical domain Ω with prescribed traction $\mathbf{t}_0$ along the Neumann boundary Γ_t and prescribed displacements $\mathbf{u}_0$ along the Dirichlet boundary Γ_u, (b) extended domain $\Omega_{FD}\backslash\Omega$ with zero traction $\mathbf{t}_0$ on the cell domain surface $\partial\Omega_{fict}$, (c) embedded domain with implicit domain support for Ω_{fict} from prescribed displacement constraints on Γ_u and (d) finally applied cell grid structure on Ω_{ext} with location function $\alpha(\mathbf{x})$.

Scaling $\mathbf{C}$ by a location dependent factor $\alpha(\mathbf{x})$ penalizes stresses in the fictitious domain and retains the full contribution of stresses in the true solution domain.

$$\boldsymbol{\sigma} = \alpha(\mathbf{x})\, \mathbf{C}\, \boldsymbol{\epsilon} \tag{10}$$

with

$$\alpha(\mathbf{x}) = \begin{cases} \alpha = 1 & \forall\, \mathbf{x} \in \Omega \\ \alpha = \gamma & \forall\, \mathbf{x} \in \Omega_{ext} \backslash \Omega \end{cases} \tag{11}$$

The value for γ is chosen smallest possible to confine the influence of the extension domain but to ensure sufficient numerical stability w.r.t. the conditioning of the governing system of equations. Typical values for γ range between 10^{-14} and 10^{-4}. According to the stresses in (10), volume loads are penalized with the same $\alpha(\mathbf{x})$ to restrict them to the solution domain Ω.

Using (10) and (11), the weak form of the elasticity problem on Ω remains a consistent formulation of the principle of virtual work:

$$\int_{\Omega_{\text{ext}}} \delta\, \boldsymbol{\epsilon}^T \alpha\, \mathbf{C}\, \boldsymbol{\epsilon}\, dv = \int_{\Omega_{ext}} \delta\, \mathbf{u}^T \alpha\, \mathbf{p}\, dv + \int_{\Gamma_u} \delta\, \mathbf{u}^T \mathbf{t}_0\, da$$

$$x \in \Gamma_u \;\Rightarrow\; \mathbf{u} = \mathbf{u}_0 \tag{12}$$

with $\boldsymbol{\epsilon}$ and $\boldsymbol{\sigma}$ representing the strain and stress vectors in Voigt notation, $\mathbf{u}$ the displacement vector and $\mathbf{p}$ the volume load vector.

The absence of boundary fitted elements in the finite cell method requires a weak enforcement of the essential boundary conditions. A Nitsche-like approach showed excellent performance properties for the voxel-based models. A detailed description of the applied approach can be found in (Ruess et al. 2012) and (Ruess et al. 2013).

The hexahedral finite cells are implemented according to the principles of the tensor product elements of the finite element method. The unknown displacement field $\mathbf{u}(\mathbf{x})$ is approximated with hierarchical piecewise defined polynomials of higher order $\mathbf{N}_i(\xi,\eta,\zeta)$ specified in the standard hexahedral $(-1 \le \xi,\eta,\zeta \le 1)$.

$$\mathbf{u} = \textstyle\sum_a \mathbf{N}_a(\xi,\eta,\zeta)\mathbf{U}_a \tag{13}$$

$$\delta\mathbf{u} = \textstyle\sum_a \mathbf{N}_a(\xi,\eta,\zeta)\, \delta\mathbf{U}_a \tag{14}$$

with $\mathbf{U}_a$ denoting the unknown degrees of freedom and corresponding virtual components. The approximation of the linear strain tensor $\boldsymbol{\epsilon}$ and corresponding virtual quantity, applies the standard strain operator $\mathbf{B}(\xi,\eta,\zeta)$ that is obtained from differentiation of (13) with respect to the global coordinates (x,y,z), applying the chain rule.

Following the Bubnov-Galerkin approach equations (13) and (14) are substituted into the weak form (11) providing a discrete finite cell formulation

$$\mathbf{K}\, \mathbf{U}_a = \mathbf{P} \tag{15}$$

with the (N×N)-matrix $\mathbf{K}$ representing system stiffness and system load vector $\mathbf{P}$.

4.1 *Evaluation of a homogenized Young's modulus*

The fictitious domain approach is adjusted for voxel data sets. Instead of an explicit separation between the domain of interest Ω and the fictitious extension domain Ω_{ext} the various sub-domains and corresponding interfaces are given implicitly by the voxel value distribution. The penalization of stresses and forces is set into a direct relation to the value of each voxel and thus is adjusted to the heterogeneity of the material data.

We use an isotropic heterogeneous material model to determine the elasticity response, having at each point a different Young's modulus in the trabecular bone, depending on the local density. The density values are obtained in Hounsfield Units (HU) and further transformed in BMD values as explained in Section 2.

The Poisson ratio was chosen at $\nu = 0.3 = \text{const}$. The governing integrals of (12) for the stiffness matrix and the external forces are solved by a composed integration scheme that is capable to exploit a pre-computation of an essential part of the applied Gauss quadrature scheme. The integral is split into a set of integrals over sub-domains that fully cover the integration domain. The regular grid structure of the voxel data (Fig. 11) is favorably used for the decomposition process such that each voxel is represented by a sub-domain cell. This way the material properties of each voxel according to the predefined material model are included into the material distribution. A detailed description of the composed integration process for voxel-based models can be found in (Yang et al. 2012).

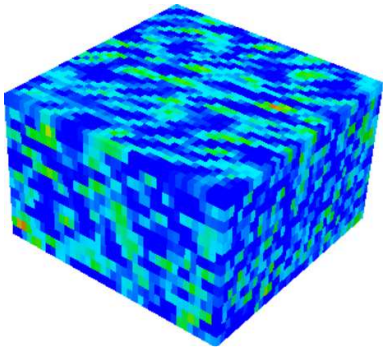

Figure 11. HU distribution of a voxel sample cube.

The elasticity properties of the sample cubes are determined from prescribed unit strain states $\epsilon_{ij} = \mathbf{e}_i \mathbf{e}_j^T$ (i,j=1,2,3). Symmetry boundary conditions were applied at three adjacent faces. At the remaining faces prescribed displacements were applied to ensure the unit strain states ϵ_{ij}. For each load case the stress response is simulated with a discretization of 5×5×2 finite cells at a polynomial degree p=3. The cell stiffness integration includes the elasticity properties at each voxel due to the sub-cell quadrature. With the analysis results the state of stress $\langle \sigma_{ij} \rangle$ is evaluated at each voxel position $\mathbf{x}$ for the given material values $E(\mathbf{x})$. A spatial averaging over all stress contributions for each load case reveals the macroscopic homogenized stress components $\bar{\sigma}_{ij}$ (Kanit et al. 2006).

$$\bar{\sigma}_{ij} = 1/V \int_V \sigma_{ij}\, dv \tag{16}$$

The apparent elasticity components of the material tensor follow from (16) evaluated for the unit strain states.

5 RESULTS

The methodology presented in this paper has been applied to the estimation of the average elasticity modulus in the three main directions for 300 simulated bone samples according to the algorithm proposed in Section 3.4 and using the FCM as explained in Section 4. The simulated bone samples had a size of 7.3×7.3×6.7 mm^3 with the same resolution as the experimental samples (Table 1) and the domain was divided in $M = 500$ blocks of equal size. The largest positive $N = 20$ eigenvalues of the covariance matrices $\Sigma^{(i)}$ were used in each iteration of the algorithm and the value of the negligible correlation was $\xi = 0.01$.

To define the mapping between density ρ and elasticity modulus E, we applied different models, namely the ones developed by Wirtz (Wirtz et al. 2000), Cody (Cody et al. 2000), Lotz (Lotz et al. 1990), and Keller (Keller 1994). These models were established based on tests conducted at the scale of the simulated bone samples. To the knowledge of the authors, a material model has not been yet developed based on evidence at the scale of the voxels. Analytical expressions of each model are summarized in (Yosibash et al. 2007). The models are expressed in terms of the apparent dry density ρ_{app} [g/cm^3] (Keller 1994), which is expressed in terms of the bone mineral density ρ_{BMD} [g/cm^3], as follows:

$$\rho_{ash} = 1.22\rho_{\text{BMD}} + 0.0523 \tag{17}$$

$$\rho_{app} = \begin{cases} \frac{\rho_{ash} - 0.007}{0.522}, & \rho_{ash} < 0.529 \\ \frac{\rho_{ash} + 0.25}{0.779}, & \rho_{ash} \geq 0.529 \end{cases} \tag{18}$$

where ρ_{ash} [g/cm^3] is the ash density (Keller 1994).

A first comparison between the experimental elasticity modulus and the corresponding output of the different material models using the average bone density of each simulated sample is shown in Figure 12. A good agreement between experiment and simulation based on all models was obtained. This is explained by the fact that the applied material models are used at the sample scale, corresponding to the average density of the samples.

If the material models are used at each scanned location of the sample (i.e. at the voxel scale) and the elasticity modulus is evaluated by homogenization applying FCM (Section 4.1) then the discrepancy between the experimental and theoretical estimations increases considerably (Fig. 13).

Figures 12 and 13 show how models that are accurate for the estimation of the elasticity modulus in the sample scale are not necessarily applicable at the voxel scale. Therefore, different relations need to be established for the mapping of bone density to elasticity modulus at the voxel scale to obtain better agreement with laboratory tests.

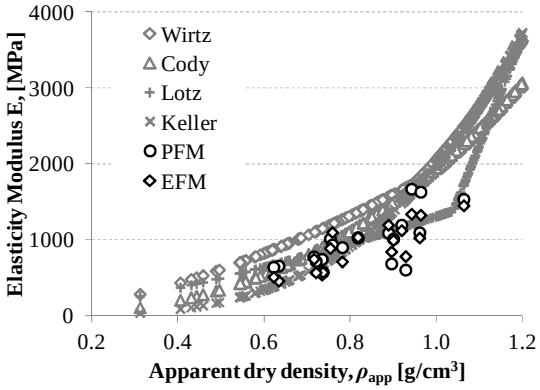

Figure 12. Experimental (PFM and EFM) and estimated (Wirtz, Cody, Lotz and Keller) elasticity modulus using the average bone density of the simulated samples (i.e. macro-scale).

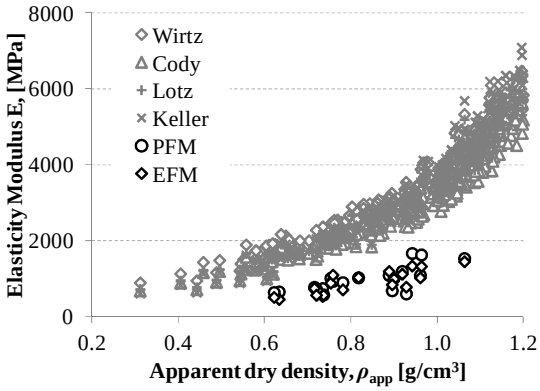

Figure 13. Estimated elasticity modulus using the FCM and the (Wirtz, Cody, Lotz and Keller) material models in the voxel scale and experimental results (PFM and EFM).

6 CONCLUSION

A probabilistic model of the bone density of the trabecular region of fresh-frozen human femurs was combined with the Finite Cell Method (FCM) for the simulation of bone samples and the estimation of their elasticity moduli. A novel algorithm based on a sequential Gaussian simulation using a truncation of the spectral decomposition of the random field defined by the bone density was developed to generate the random bone samples. The FCM was applied for the estimation of the average elasticity modulus of the random samples. Comparison between the estimated and experimental elasticity modulus is presented using different material models. On the one hand, very good agreement is observed when the material models are applied to the average density of each sample. This is due to the fact that the material models were derived based on tests conducted at the sample scale. On the other hand, the comparison shows significant deviation between experimental and simulated results when the material models are applied at the voxel level. This suggests the need for the development of different material models for application at this scale.

ACKNOWLEDGEMENTS

The authors thank Eduardo Grande García for useful discussions and for sharing his insights into the performed experiments and the characteristics of the data.

REFERENCES

Cody D, Hou FJ, Divine GW, Fyhrie DP, 2000. Short term in vivo study of proximal femoral finite element modeling. *Annals Biomedical Engineering* 28, 408–414.

Grande E, 2013. Double Experimental Procedure for Model-Specific Finite Element Analysis of the Human Femur and Trabecular Bone. PhD thesis, Technische Universität München.

Kanit T, Guyen FN, Forest S, Jeulin D, Reed M, Singleton S, 2006. Apparent and effective physical properties of heterogeneous materials: Representativity of samples of two materials from food industry. *Computer Methods in Applied Mechanics and Engineering*, 195, pp 3960–3982.

Keller T, 1994. Predicting the compressive mechanical behavior of bone. *Journal of Biomechanics* 27, 1159–1168.

Lotz JC, Gerhart TN, Hayes WC, 1990. Mechanical properties of trabecular bone from the proximal femur: a quantitative CT study. J. Comput. Assist. Tomogr., 14(1), pp. 107–114.

Ruess M, Schillinger D, Bazilevs Y, Varduhn V, Rank E, 2013.Weakly Enforced Essential Boundary Conditions for NURBS-embedded and trimmed NURBS geometries on the basis of the Finite Cell Method. *accepted for publication, Int'l Journal for Numerical Methods in Engineering*.

Ruess M, Tal D, Trabelsi N, Yosibash Z, Rank E, 2012. The finite cell method for bone simulations: Verification and validation. *Biomechanics and Modeling in Mechanobiology* 11(3): 425-437.

Schillinger D, Ruess M, Zander N, Bazilevs Y, Düster A, Rank E, 2012. Small and large deformation analysis with the p- and B-spline versions of the Finite Cell Method. *Computational Mechanics* 50(4): 445-478.

QCT PRO™ 2008. Bone Mineral Densitometry Software, CT Calibration Phantom. Mindways Software, Inc. Version 4.2.3 – Revision 20070717C.

Vanmarcke, E. 2010. *Random Fields, Analysis and Synthesis*. World Scientific Publishing.

Wirtz DC, Schiffers N, Pandorf T, Radermacher K, Weichert D, Forst R, 2000. Critical evaluation of known bone material properties to realize anisotropic FE-simulation of the proximal femur. Biomechanics 33, pp. 1325–1330.

Yang Z, Ruess M, Kollmannsberger S, Düster A, Rank E, 2012. An efficient integration technique for the voxel-based Finite Cell Method. *Int'l Journal for Numerical Methods in Engineering*, 91(5), pp 457-–471.

Yosibah Z, Padan R, Joskowicz L, Milgrom C, 2007. A CT-based high-order finite element analysis of the human proximal femur compared to in-vitro experiments. Biomechanical Engineering 129(3), pp 297-309.